



Full paper

NiO@carbon spheres: A promising composite electrode for scalable fabrication of planar perovskite solar cells at low cost

Sajid Sajid^{a,1}, Ahmed Mourtada Elseman^{b,*,1}, Dong Wei^a, Jun Ji^a, Shangyi Dou^a, Hao Huang^a, Peng Cui^a, Meicheng Li^{a,*}

^a State Key Laboratory of Alternate Electrical Power, System with Renewable Energy Sources, School of Renewable Energy, North China Electric Power University, Beijing 102206, China

^b Electronic & Magnetic Materials Department, Advanced Materials Division, Central Metallurgical Research and Development Institute (CMRDI), Helwan, P.O. Box 87, Cairo 11421, Egypt



ARTICLE INFO

Keywords:

NiO@CSs-composite
Organic hole-conductor free
Metal-electrode free
Perovskite solar cell

ABSTRACT

Efficiencies of perovskite solar cells (PSCs) are now hitting such high levels that scalable fabrication at low-cost is becoming pivotal. However, this remains challenging due to expensive metal electrodes and organic hole-transporting materials (OHTMs) typically used in PSCs. By simplifying the device structure, OHTMs-free and noble metal-electrodes-free planar PSCs with the aperture area of 1 cm² are fabricated with novel NiO@CSs-composite electrodes. The distribution of hole-accepting nickel oxide (NiO) as closely-packed shells on the core carbon spheres (CSs) in the rambutan-like NiO@CSs-composite enhances the photogenerated hole collection efficiency and reduces recombination loss. The small porosity of this composite inhibits the intrusion of the oxygen/moisture through the counter electrode, thus enabling a stable device's efficiency of 11.70% up to 1500 h under 40–60% humidity without encapsulation. The ability to fabricate large-sized planar devices with NiO@CSs-composite electrodes represents a significant step towards the cost-effective and scalable manufacturing with numerous possibilities to choose and optimize the materials, and device's architecture.

1. Introduction

Organic-inorganic trihalide perovskites (MAPbX₃; MA = CH₃NH₂, X = I, Cl, Br) have been emerged as promising light-harvesting semiconductors for solution-processable photovoltaic devices [1]. Miyasaka and co-workers reported the first overture of perovskite solar cell (PSC) with a power conversion efficiency (PCE) of 3.8% [2]. Since then, high PCEs in the range of 20–22% have been obtained in PSCs through compositional engineering of perovskites [3–5], high-quality film formation techniques [6–8], and improved device structure [9–12]. Now, simultaneously requirements of low-cost and simplified fabrication route for stable PSCs are guidelines to promote the industrial production.

Despite the efforts for boosting device's efficiencies, there are certain concerns about the cost and high-temperature processing of PSCs that can potentially hinder their large-scale applications [13–15]. The high-cost originates from the tedious synthetic protocols and high-purity requirements of the OHTMs (i.e. spiroOMeTAD or PTAA) and precious metal-electrodes (Au or Ag) typically used in PSCs. The high-

annealing temperatures, particularly for the mesoscopic devices increase the energy consumption and fabrication processes [16]. One strategy to combat the issue of cost could be the use of inexpensive counter electrodes (such as Ni and carbon) and OHTMs-free PSCs [17–19]. However, the OHTMs-free or carbon based PSCs are frequently fabricated with high-sintered scaffolds of TiO₂, ZrO₂, Al₂O₃ or NiO, followed by a precise control of perovskites infiltration [20–24]. In these mesoporous layers the insertion of NiO showed better device's performance due to suppressed charge recombination [25]. In addition, the incorporation of NiO nanoparticles into carbon electrodes (single-walled carbon nanotube or carbon-black/graphite) also assured effective hole extraction at the interface between perovskite-layer and back-electrodes [26]. Even though high photovoltaic performances were obtained, the expensive synthetic methods for carbon nanotubes and high-sintering processes for mesoporous layers increase the cost and energy consumption in the fabrication of these solar cells [20]. Among various inorganic charge transporting materials, NiO is an extremely cheap, abundant p-type semiconductor that exhibits wide bandgap, high-hole mobility, good thermal and chemical stability, and suitable

* Corresponding authors.

E-mail addresses: amourtada@cmrdi.sci.eg (A.M. Elseman), mcli@ncepu.edu.cn (M. Li).

¹ These authors contributed equally to this work.

energetic landscapes with perovskites and carbon material [25,27]. The fabrication of low-temperature-processed devices with low-cost NiO/carbon-based electrode would foster the large-scale deployment of PSCs [28]. In this context, our previous theoretical simulation results showed that the appropriate integration of NiO and carbon composite can work as an efficient electrode in the planar PSCs [29].

In this report, we develop a simple and cost-effective strategy for the synthesis of nickel oxide and carbon spheres composite, which acts as an efficient counter electrode in planar PSCs. The incorporation of NiO at carbon spheres (NiO@CSs-composite) enhances the conductivity of carbon-electrode and the electronic contact with perovskite layer. We use the doctor-blading method to fabricate NiO@CSs-composite electrode at low-temperature in planar PSCs with an aperture area of 1 cm² for the first time. The high hole-mobility (640.7–751.34 cm² V⁻¹s⁻¹) and favorable energetic landscapes of this composite are beneficial for hole transport and extraction, and thus resulting in retard charge carrier recombination. Furthermore, devices based on NiO@CSs-composite have low-cost and simplified fabrication processes as no expensive electrodes, OHTMs, and high-sintering temperature are required. The best device exhibits a V_{OC} of 0.84 V, J_{SC} of 22.056 mA cm⁻², FF of 63.155%, and a stable PCE of 11.70% up to 1500 h at 40–60% humidity without encapsulation. This work offers higher flexibility to choose and optimize the architecture of the device, as well as investigate the new materials for the carbon-based electrodes.

2. Experimental section

All the analytical grade reagents were commercially obtained and used without further purification.

2.1. Synthesis of carbon spheres (CSs)

All the analytical grade reagents were commercially obtained and used without further purification. Carbon spheres (CSs) were prepared by hydrothermal synthesis from glucose precursor according to literature [30,31]. An aqueous sucrose solution of 0.7 mol/L was added into a stainless-steel autoclave with a total volume of 50 mL. The autoclave was preheated in an oven at 250 °C about 12 h. After cooling the autoclave to room temperature, the suspension was centrifuged for 5 min at 5000 rpm. The product was then purified by five more centrifugation/re-dispersion steps with deionized water and anhydrous ethanol, and finally dried at 60 °C in an oven.

2.2. Synthesis of NiO@CSs-composite

The NiO@CSs-composite were synthesized via one-step synthetic method as depicted in Fig. S1 (Supporting information). Different weight ratio (w/w) from as-prepared carbon spheres to nickel(II) acetate [Ni(CH₃CO₂)₂] were prepared (i.e. 1:9, 1:4, and 3:7). The CSs were ultrasonically dispersed into 100 mL of deionized water for 30 min. Then, 0.6 g of ethylene glycol and 2.09 g of Ni(CH₃CO₂)₂ were added into the previous solution. Homogeneous mixture was obtained with stirring for 2 h. Next, the previous solution was transferred to a Teflon-lined stainless-steel autoclave and heated in an oven at 200 °C for 24 h. Afterwards, the precipitates were collected by centrifugation, washed with deionized water for several times, then dried at 60 °C overnight to obtain NiO@CSs-composite.

2.3. Preparation of NiO@CSs-composite paste

1.2 g of NiO@CSs-composite were dispersed in 13 mL ethyl alcohol followed by ultrasonication for 20 min. This solution was further treated by an ultrasonic bath for 20 min. Later on, 15 mL terpineol was added to the solution. The mixture was then treated by ultrasonic for another 5 min, ball-milling for 3 h with 500 rpm. Finally, 10 g of ethyl cellulose was added into the solution. In the last step, the ethyl alcohol was removed with rotary evaporation.

2.4. Fabrication of perovskite solar cells

Fluorine-doped tin oxide substrates were cleaned by sequential ultrasonication with a detergent solution, deionized water, acetone, and isopropyl alcohol for 20 min, respectively. After dried by a nitrogen flow, the substrates were subjected to an O₃/ultraviolet treatment for 15 min before use. After cleaning the glass substrates, an aqueous stock solution of 2 M TiCl₄ (stored in the freezer) was diluted to the required concentration [32]. The electrodes were then immersed into this solution and kept in an oven at 70 °C for 1 h in a closed vessel. After 1 h the electrodes were washed with deionized water and ethanol, and then dried at 100 °C in air for an hour to obtain hole-blocking layer of TiO₂. A slightly modified one-step solution method than the previously reported literature [33] was used for the CH₃NH₃PbI₂Cl-film formation under open atmosphere with consecutive diethyl ether dripping. The precursor containing 159 mg CH₃NH₃I, and 461 mg PbCl₂ in anhydrous DMF/DMSO (600 μl/78 μl) solution was spin-coated on c-TiO₂-coated substrate at 4000 r.p.m. for 30 s. During the spinning process, 0.5 mL diethyl ether as anti-solvent was slowly poured to rush the film. After being annealed at 130 °C for 10 min, a black film of perovskite layer was formed. Finally, the back-electrode was fabricated by doctor blading the as-prepared paste of NiO@CSs-composite, followed by annealing at 50 °C for 15 min.

2.5. Characterization of NiO@CSs-composite and as-prepared devices

The X-ray diffraction (XRD) was carried out by Rigaku TTR-III diffractometer at 2θ ranges from 10° to 90° using Cu-K α radiation (wavelength λ = 1.5418 Å). Raman spectra were tested by a Renishaw inVia Raman microscope at room temperature with a 514 nm wavelength laser excitation. The morphology was investigated by a scanning electron microscopy (SEM, XL30ESEM-TMP) and transmission electron micrographs instrument (TEM, JEM-2100). X-ray photoelectron spectroscopy (XPS, ESCALAB 250) was measured at room temperature, Al Ka X-ray beam was adopted as the excitation source with a power of 250 W, the vacuum pressure of instrument chamber was kept at 1 × 10 Pa, and the bonding energy was calibrated with reference to C 1s peak (285.0 eV). The hole-mobility and conductivity measurements were carried out by Nanometrics HL5500 Hall System. Current-voltage (J – V) characteristic curves were measured using a source meter (Keithley 2400) under AM 1.5G irradiation with a power density of 100 mW/cm² from a solar simulator (XES-301S + EL-100). The steady PL spectra were performed by a spectrometer (Edinburg PLS 980). The IPCE was measured by using QER systems (Enli Tech.).

3. Results and discussion

The powder X-ray diffraction (XRD) experiments were performed to determine the crystal structures of NiO@CSs-composite as shown in Fig. S2 (Supporting information). From the XRD pattern of as-prepared NiO@CSs-composite, a broad peak around 24.5° corresponds to the (002) diffraction mode of graphitic structure, indicating glucose were successfully carbonized under the hydrothermal process. Pure NiO in Fig. S2 exhibits five well-defined peaks at 37.2°, 43.3°, 62.8°, 75.4°, and 79.3°, respectively. This can be well indexed as (111), (200), (220), (311) and (222) crystal planes of cubic NiO (JCPDS: 71-1179). Importantly, the broader and weaker diffraction peaks of NiO@CSs-composite (Fig. 1b) are located at the same positions as for pure NiO [30,31].

The structural features of pure NiO and as-prepared NiO@CSs-composite were investigated by Raman spectroscopy. The Raman spectrum of pure NiO (Fig. S2) shows two peaks around 500 and 1090 cm⁻¹, corresponding to the first- and second-order longitudinal optical phonon modes of Ni-O bond. Besides NiO mode at 500 cm⁻¹, the NiO@CSs-composite indicates the D-band around 1321 cm⁻¹ and G-band around 1582 cm⁻¹ as shown in Fig. S2, which are typical bands

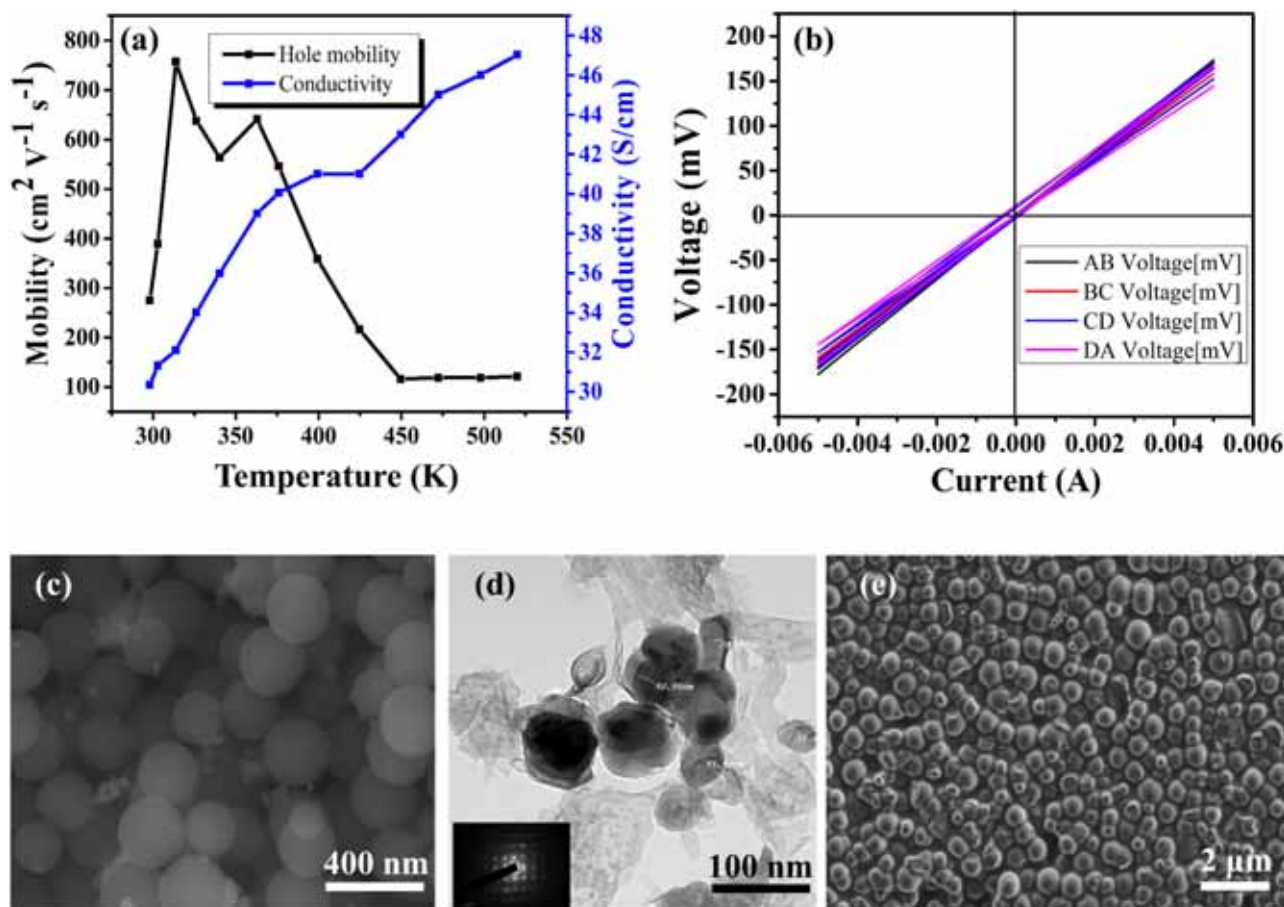


Fig. 1. (a) Hole-mobility and conductivity measurements. (b) The current–voltage (I – V) curves between each pair of contacts AB, BC, CD and DA for the NiO@CSs-composite thin film. (c, d) SEM and TEM images of NiO@CSs-composite powder. (e) Top-view SEM image of NiO@CSs-composite film.

of carbonaceous materials. The Raman spectrum of NiO@CSs-composite strongly confirms the successful integration of NiO and carbon spheres [34,35].

The X-ray photoelectron spectroscopy (XPS) was conducted to determine the chemical compositions and corresponding valence states of NiO@CSs-composite. As shown in Fig. S3 (Supporting information), the spectrum survey reveals that NiO@CSs-composite are completely composed by Ni, O, and C elements [36]. The C 1s spectrum is indicated around 285 eV. The Ni 2p spectra of NiO@CSs-composite shows curves with two strong peaks around 854.2 and 872.7 eV, which assigned to Ni 2p_{3/2} and Ni 2p_{1/2} spin orbits, indicating the character of Ni⁺² and Ni⁺³ in NiO crystal (Fig. S3) [37]. These results further suggesting that NiO is successfully embedded in the carbon spheres.

The electronic properties of NiO@CSs-composite were investigated through Hall-effect measurements. The Hall-effect measurements have been elucidated as an important characterization for semiconductor materials [38]. These features include Hall voltage, type of semiconductor, carrier density, and Hall mobility. In addition, measuring mobility is especially important for designing efficient photovoltaic devices. Mobility strongly depends on the nature of the material, its structure, and purity. Herein, we investigate the Hall mobility and conductivity of NiO@CSs-composite as a function of temperature as depicted in Fig. 1(a). It can be seen that the hole mobility (μ_h) gradually increases at low temperature and becomes maximum about 751.34 cm² V⁻¹ s⁻¹ at 313 K [39]. Then, this value drop to 640.7 cm² V⁻¹ s⁻¹ at 363 K. After this point, it was found that the hole mobility is decreased to 100 cm² V⁻¹ s⁻¹ at 450 K and then remained constant with increasing temperature. On the other hand, the conductivity (σ) is dominated by the gradually increasing temperature. The change in

conductivity was attributed to the movement of electron-hole pairs because at high temperature the covalent bonds were broken and as a result more electron-hole pairs were available for conduction. In other words, with increasing temperature, the electrons from valence band acquired energy and jumped to conduction band. The positive sign of Hall coefficient in Hall-effect measurement showed the similar p-type semiconductor's behaviour. The semiconductor feature was also confirmed by the current–voltage (I – V) curves between each pair of contacts AB, BC, CD and DA at different temperatures between 295 and 522 K (Fig. 1(b)). In all cases, the linearity of I – V curves describe suitable Ohmic contacts [40,41].

Furthermore, the scanning electron microscopy (SEM) and tunneling electron microscopy (TEM) analyses were carried out to investigate the morphology of NiO@CSs-composite. The SEM image of NiO@CSs-composite in Fig. 1(c) shows obvious rough spherical feature with a size of 400 nm in a large-scale domain. The TEM image in Fig. 1(d) reveals a large number of NiO nanoparticles that surround the carbon spheres and form a typical core-shell structure, and exhibit a rambutan-like structure. Here, the presence of NiO nanoparticles could effectively increase the electrical kinetics and enable the fabrication of dense layer owing to the small particle size. The SEM image with large scale was then used to inspect the quality of NiO@CSs-composite film prepared by doctor-blading technique. As shown in Fig. 1(e), the majority of the as-prepared composite are packed together to form a dense layer. This is critical for achieving high film coverage on top of perovskite. From these structural and morphological investigations, it clearly demonstrates the advantage of NiO@CSs-composite electrode in PSCs.

Based on high hole-mobility, small size porosity and favorable energy band alignment with perovskite, we have employed NiO@CSs-

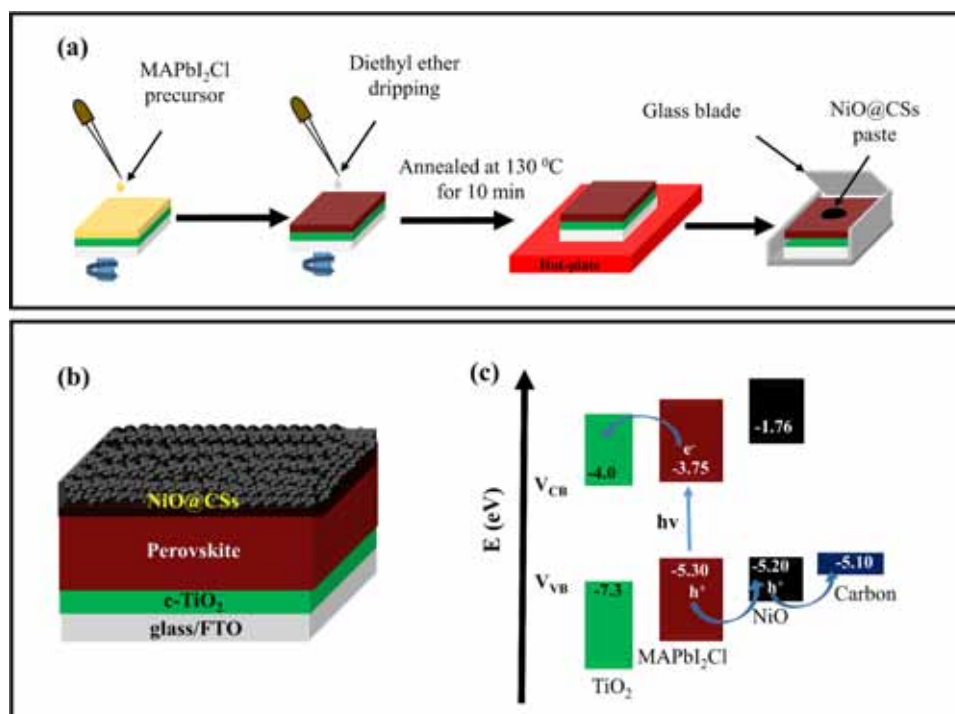


Fig. 2. Schematic representations of (a) Perovskite solar cell fabrication. (b) Device configuration. (c) Energy band diagram of the corresponding materials.

composite as counter electrode to combine with CH₃NH₃PbI₂Cl (CH₃NH₃PbI₂Cl denoted as MAPbI₂Cl thereafter) for fabricating low-temperature-processed planar PSCs, as illustrated in Fig. 2(a). Since the formation of a compact NiO@CSs-composite electrode that can provide better interfacial contact with MAPbI₂Cl-film is essential to avoid shunting and accelerate the extraction of charge carriers, it is critical to control the integration of NiO and carbon spheres (CSs). In this context, the smaller size of NiO in CSs with different weight ratio (w/w) from starting materials were taken (1:9, 1:4, and 3:7) to obtain small porosity of NiO@CSs-composite.

A thin layer of compact-TiO₂ (c-TiO₂) was first fabricated over glass/FTO substrate according to our previous reports [42,43]. Then, a dense film of perovskite was spin-coated on FTO/c-TiO₂ substrate. Finally, the device fabrication was completed (Fig. 2(b)) by doctor-blading the NiO@CSs-composite electrode. From the energy level diagram (Fig. 2(c)), the dissociated charge carriers (electrons and holes) in the MAPbI₂Cl perovskite can be extracted and transferred efficiently to the c-TiO₂ and NiO@CSs-composite electrode. Since NiO has a fairly well-matched energy level with the MAPbI₂Cl and with the work function of carbon, a proper Ohmic contact is expected.

To elucidate the role of NiO@CSs-composite as counter electrode, steady-state photoluminescence (PL) and time-resolved PL decay experiments were adopted to compare the hole injection efficiency from the MAPbI₂Cl-layer to pure CSs and different weight ratio of CSs to NiO (1:9, 1:4, and 3:7) as depicted in Fig. 3(a, b). The layer with NiO@CSs-composite (1:4 w/w) exhibits more efficient PL quenching compared to pure CSs and other weight ratio. The lower performance could be attributed to the voids present in the films, random walk of charge carriers, and inefficient hole collection by the as-prepared layers. Compared to other weight ratio of CSs to NiO (1:9 and 3:7 w/w) in the composite, the enhanced hole extraction should be the result of suppressed voids, improved interfacial contact and effective hole injection from MAPbI₂Cl to NiO@CSs-composite (1:4 w/w).

Time-resolved photoluminescence showed that the pristine perovskite film has a relatively long PL lifetime of 182.3 ns, while it decreased significantly to 3.34 ns for perovskite/NiO@CSs-composite (1:4 w/w) electrode. Compared to other weight ratio in the composite

electrode on MAPbI₂Cl-film, the shorten lifetime for MAPbI₂Cl/NiO@CSs-composite (1:4 w/w) indicates that the proper integration of NiO and CSs can effectively improve the charge carriers injection efficiency.

To verify the efficacy of NiO@CSs-composite as electrode, devices with the configuration of FTO/c-TiO₂/MAPbI₂Cl/NiO@CSs-composite were prepared accordingly (Fig. 2(a)). The PSC based on pure CSs, and CSs to NiO weight ratio (1:9, 1:4, and 3:7) denoted as devices A, B, C, and D, respectively. The dependence of device performance on pure CSs and different weight ratio of CSs to NiO were first investigated to identify the optimum weight ratio for the best counter electrode. The current-voltage ($J-V$) characteristic curves and incident photon-to-electron conversion efficiency (IPCE) are shown in Fig. 3(c, d), and their corresponding photovoltaic parameters data are summarized in Table 1. It was found that device-A showed current leakage and low shunt resistance due to poorer coverage on the perovskite surface, which also result in a low open-circuit voltage (V_{oc}) and small fill factor (FF). On the other hand, PSCs based on large quantity of NiO or CSs in the electrodes of devices B and D also showed low FF due to increased series resistance. The NiO@CSs-composite layer in device-C was found to be efficient with weight ratio of 1:4. The resulting PCE of the optimized device was 11.70%, which implies that NiO@CSs-composite layer with proper integration works well as back-contact.

A cross-sectional SEM image of the optimum device is shown in Fig. 4(a), where the individual layers of c-TiO₂/MAPbI₂Cl/NiO@CSs-composite can be distinguished with thicknesses of 30 nm, 650 nm, and ~4 μm, respectively. The photovoltaic performance obtained from the optimum device-C are presented in Fig. 3(c), which achieve a J_{sc} of 22.056 mA cm⁻², a V_{oc} of 0.84 V, a FF of 63.155%, leading to an overall PCE of 11.70%. The higher V_{oc} could be due to the better energy levels alignment at NiO@CSs-composite/perovskite interface, which minimizes the charge-extraction barrier and enlarges the built-in potential across the solar cell. Additionally, the enhanced J_{sc} and FF can be interpreted as the consequences of efficient hole extraction and electron blocking capability of the NiO@CSs-composite electrode, which is reflected in the corresponding improvement in the IPCE measurements (Fig. 3(d)).

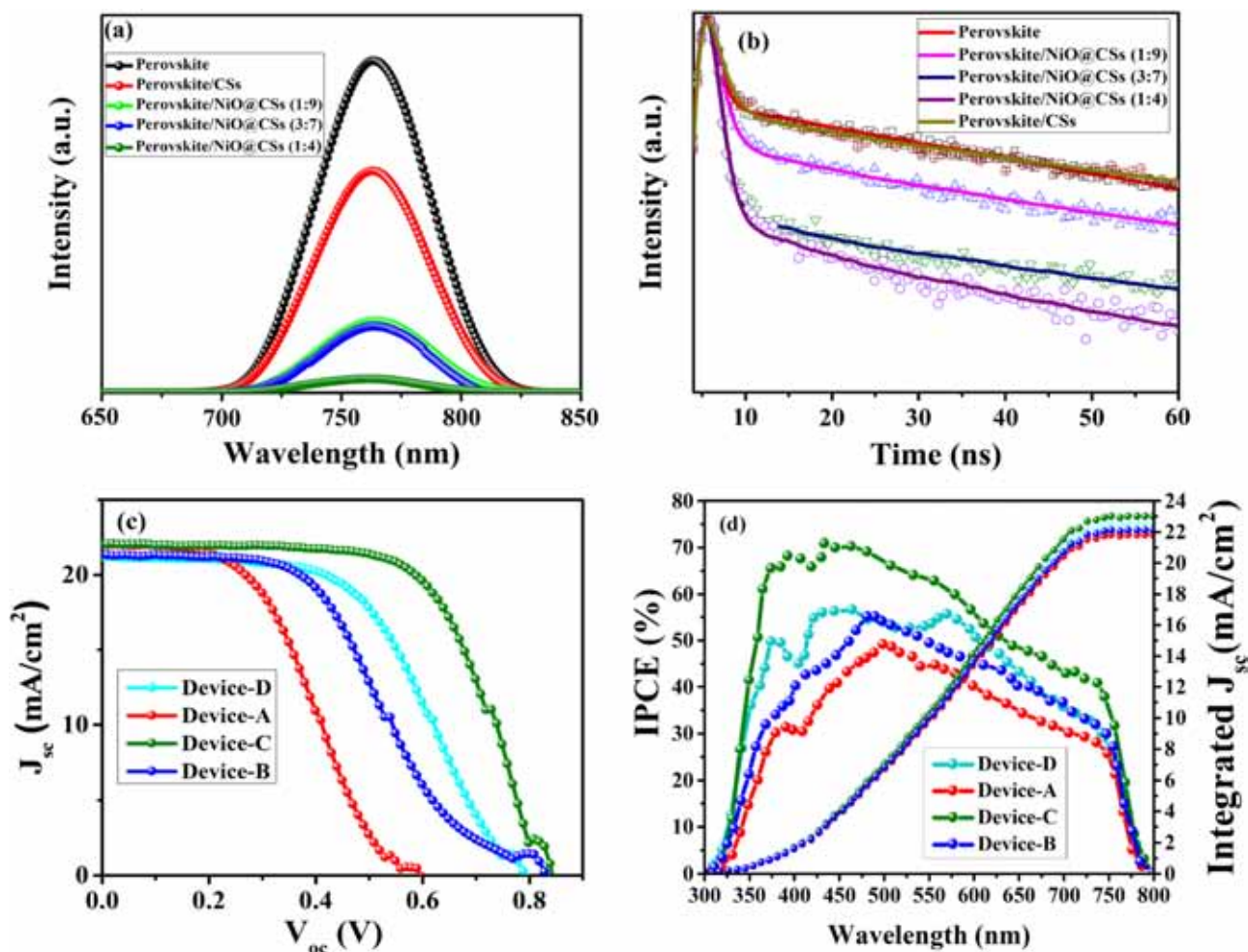


Fig. 3. (a, b) The steady-state photoluminescence spectra and time-resolved PL decay of pure MAPbI₂Cl-perovskite, MAPbI₂Cl-coated layers of carbon spheres and different weight ratio of carbon spheres to nickel oxide in NiO@CSs-composite electrode. (c) Current-voltage characteristic curves of the corresponding devices. (d) Incident photon-to-electron conversion efficiency with integrated current density.

Table 1

Photovoltaic parameters of the prepared PSCs under the illumination of AM 1.5G, 100 mW/cm².

Device	J_{sc} (mA cm ⁻²)	Integrated J_{sc} (mA cm ⁻²)	V_{oc} (V)	FF (%)	PCE (%)
A	22.019	21.8	0.59	43.028	5.59
B	21.35	22.04	0.83	43.228	7.66
C	22.056	22.90	0.84	63.155	11.70
D	21.20	22.35	0.79	53.06	8.89

Stability is a critical concern for PSCs because the intrinsic affinity of organometal halide perovskites for moisture degrade their unsealed devices in humidity. Herein, we tested the stability only for the device-C because it gives best photovoltaic performance so far. The stability of the device-C by exposing it directly to the ambient environment at 25 and with 40–60% humidity without encapsulation is depicted in Fig. 4(b).

It can be seen that device-C maintains the majority of the original PCE up to 300 h, while it slightly decreases from 11.70% to 11.22% after 1500 h, showing only 0.48% loss. This long-term stability performance is attributed to the small porosity of NiO@CSs-composite owing to the smaller size of NiO on CSs, which could inhibit the intrusion of the oxygen/moisture through the counter electrode. Moreover, we have also measured the stability of power output as a function of time under a constant voltage bias at maximum power point

tracking (inset Fig. 4(b)). The PCE for the PSC based on NiO@CSs-composite rose directly to steady state and yield a maximum value of 11.70% at 0.95 V. This demonstrates that PSC prepared with weight ratio of CSs to NiO (1:4 w/w) in the composite electrode has fast charge transfer and collection across the device, resulting in the device directly reaches a steady state with respect to the voltage.

4. Conclusion

In summary, we employed cost-effective NiO@CSs-composite as counter electrode in large-sized (area of 1 cm²) planar PSCs for the first time. After hydrothermally-mixing process of NiO and CSs, the doctor-bladed NiO@CSs-composite electrode in device-C displayed a high J_{sc} of 22.056 mA cm⁻² and high V_{oc} of 0.84 V. When compared to pure CSs-based electrode in device-A, the NiO@CSs-composite exhibited a dramatic increase in FF. These results showed that the embedded-NiO is an essential part of the as-prepared electrode for obtaining high performances of carbon-based PSCs. The best device-C also maintained 96% of the original PCE's value after 1500 h at maximum power point tracking for 2000 s when exposed to ambient environment without encapsulation. Since, the prices of noble metal electrodes and OHTMs are much higher than the commercially available NiO and CSs, these results establish NiO integration in CSs as a versatile and promising route towards scalable fabrication of PSCs at low-cost, as well as offering numerous possibilities to choose and optimize the materials, and architectures of the devices. Moreover, extending the application of the

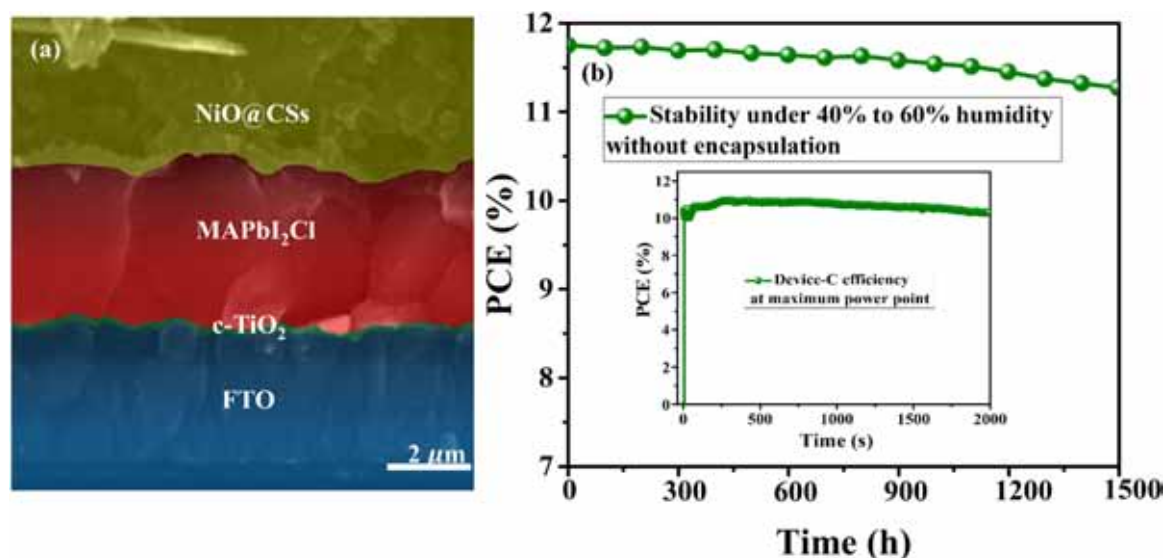


Fig. 4. (a) Cross-sectional SEM image of device-C based on NiO@CSs-composite electrode. (b) Long-term stability of device-C under ambient environment at 25 and with 40–60% humidity without encapsulation (inset is the normalized PCE at the maximum power point tracking for the optimized device-C).

NiO@CSs-composite electrode to high-quality perovskite-films formation will definitely benefit the construction of other high performance optoelectronic devices.

Acknowledgement

This work is supported partially by National Natural Science Foundation of China (Grant nos. 51772096), Beijing Natural Science Foundation (L172036), Joint Funds of the Equipment Pre-Research and Ministry of Education (6141A020225), Par-Eu Scholars Program, Science and Technology Beijing 100 Leading Talent Training Project, Beijing Municipal Science and Technology Project (Z161100002616039), the Fundamental Research Funds for the Central Universities (2016JQ01, 2017ZZD02) and the NCEPU "Double First-Class" Graduate Talent Cultivation Program.

Notes

No contending financial interest proclaim by the authors.

Appendix A. Supporting information

Supplementary data associated with this article can be found in the online version at doi:10.1016/j.nanoen.2018.11.004.

References

- J. Burschka, N. Pellet, S.-J. Moon, R. Humphry-Baker, P. Gao, M.K. Nazeeruddin, M. Grätzel, *Nature* 499 (2013) 316.
- A. Kojima, K. Teshima, Y. Shirai, T. Miyasaka, *J. Am. Chem. Soc.* 131 (2009) 6050–6051.
- J.H. Noh, S.H. Im, J.H. Heo, T.N. Mandal, S.I. Seok, *Nano Lett.* 13 (2013) 1764–1769.
- J.W. Lee, D.J. Seol, A.N. Cho, N.G. Park, *Adv. Mater.* 26 (2014) 4991–4998.
- M.A. Green, K. Emery, Y. Hishikawa, W. Warta, E.D. Dunlop, *Prog. Photovolt.: Res. Appl.* 7 (2016) 905–913.
- D. Wei, F. Ma, R. Wang, S. Dou, P. Cui, H. Huang, J. Ji, E. Jia, X. Jia, S. Sajid, *Adv. Mater.* 30 (2018) 1707583.
- D. Wei, J. Ji, D. Song, M. Li, P. Cui, Y. Li, J.M. Mbengue, W. Zhou, Z. Ning, N.-G. Park, *J. Mater. Chem. A* 5 (2017) 1406–1414.
- N.J. Jeon, J.H. Noh, Y.C. Kim, W.S. Yang, S. Ryu, S.I. Seok, *Nat. Mater.* 13 (2014) 897.
- M.M. Lee, J. Teuscher, T. Miyasaka, T.N. Murakami, H.J. Snaith, *Science* (2012) 1228604.
- H.-S. Kim, C.-R. Lee, J.-H. Im, K.-B. Lee, T. Moehl, A. Marchioro, S.-J. Moon, R. Humphry Baker, J.-H. Yum, J.E. Moser, *Sci. Rep.* 2 (2012) 591.
- P. Cui, D. Wei, J. Ji, D. Song, Y. Li, X. Liu, J. Huang, T. Wang, J. You, M. Li, *Sol. RRL* 1 (2017) 1600027.
- S. Yue, K. Liu, R. Xu, M. Li, M. Azam, K. Ren, J. Liu, Y. Sun, Z. Wang, D. Cao, *Energy Environ. Sci.* 10 (2017) 2570–2578.
- Z. Ku, Y. Rong, M. Xu, T. Liu, H. Han, *Sci. Rep.* 3 (2013) 3132.
- A. Mei, X. Li, L. Liu, Z. Ku, T. Liu, Y. Rong, M. Xu, M. Hu, J. Chen, Y. Yang, *Science* 345 (2014) 295–298.
- A.M. Elseman, D.W. Sajid, A.E. Shalan, M.M. Rashad, M. Li, Pathways towards high stable, low-cost and efficient perovskite solar cells, *Emerg. Sol. Energy Mater.* (2018) (IntechOpen).
- S. Sajid, A.M. Elseman, H. Huang, J. Ji, S. Dou, H. Jiang, X. Liu, D. Wei, P. Cui, M. Li, *Nano Energy* (2018).
- Q. Jiang, X. Sheng, B. Shi, X. Feng, T. Xu, *J. Phys. Chem. C* 118 (2014) 25878–25883.
- L. Etgar, P. Gao, Z. Xue, Q. Peng, A.K. Chandiran, B. Liu, M.K. Nazeeruddin, M. Grätzel, *J. Am. Chem. Soc.* 134 (2012) 17396–17399.
- J. Shi, J. Dong, S. Lv, Y. Xu, L. Zhu, J. Xiao, X. Xu, H. Wu, D. Li, Y. Luo, *Appl. Phys. Lett.* 104 (2014) 063901.
- Z. Li, S.A. Kulkarni, P.P. Boix, E. Shi, A. Cao, K. Fu, S.K. Batabyal, J. Zhang, Q. Xiong, L.H. Wong, *ACS Nano* 8 (2014) 6797–6804.
- L. Liu, A. Mei, T. Liu, P. Jiang, Y. Sheng, L. Zhang, H. Han, *J. Am. Chem. Soc.* 137 (2015) 1790–1793.
- H. Chen, Z. Wei, H. He, X. Zheng, K.S. Wong, S. Yang, *Adv. Energy Mater.* 6 (2016) 1502087.
- F. Zhang, X. Yang, H. Wang, M. Cheng, J. Zhao, L. Sun, *ACS Appl. Mater. Interfaces* 6 (2014) 16140–16146.
- Y. Yang, J. Xiao, H. Wei, L. Zhu, D. Li, Y. Luo, H. Wu, Q. Meng, *RSC Adv.* 4 (2014) 52825–52830.
- S. Liu, K. Cao, H. Li, J. Song, J. Han, Y. Shen, M. Wang, *Sol. Energy* 144 (2017) 158–165.
- L. Chu, W. Liu, Z. Qin, R. Zhang, R. Hu, J. Yang, J. Yang, Xa Li, *Sol. Energy Mater. Sol. Cells* 178 (2018) 164–169.
- S. Sajid, A.M. Elseman, J. Ji, S. Dou, D. Wei, H. Huang, P. Cui, W. Xi, L. Chu, Y. Li, *Nano Micro Lett.* 10 (2018) 51.
- Z. Liu, B. Sun, X. Liu, J. Han, H. Ye, Y. Tu, C. Chen, T. Shi, Z. Tang, G. Liao, *J. Mater. Chem. A* 6 (2018) 7409–7419.
- A. Elseman, J. Ji, S. Dou, H. Huang, P. Cui, D. Wei, M. Li, *Chin. Phys. B* 27 (2018) 017305.
- S. Tang, Y. Tang, S. Vongehr, X. Zhao, X. Meng, *Appl. Surf. Sci.* 255 (2009) 6011–6016.
- A.M. Hassan, A.M. Nassar, N.M. Ibrahim, A.M. Elsamman, M.M. Rashad, *J. Coord. Chem.* 66 (2013) 4387–4398.
- D. Song, P. Cui, T. Wang, D. Wei, M. Li, F. Cao, X. Yue, P. Fu, Y. Li, Y. He, *J. Phys. Chem. C* 119 (2015) 22812–22819.
- C.-H. Chiang, J.-W. Lin, C.-G. Wu, *J. Mater. Chem. A* 4 (2016) 13525–13533.
- J. Zhang, D. Zeng, S. Zhao, J. Wu, K. Xu, Q. Zhu, G. Zhang, C. Xie, *Phys. Chem. Chem. Phys.* 17 (2015) 14903–14911.
- H. Zhang, D. Guo, J. Zhu, Q. Li, L. Chen, T. Wang, *Electrochim. Acta* 152 (2015) 378–382.

- [36] H. Zhang, T. Kuila, N.H. Kim, D.S. Yu, J.H. Lee, *Carbon* 69 (2014) 66–78.
- [37] G. Chen, H. Guan, C. Dong, X. Xiao, Y. Wang, *J. Phys. Chem. Solids* 98 (2016) 209–219.
- [38] B. Stjerna, C.G. Granqvist, A. Seidel, L. Högström, *J. Appl. Phys.* 68 (1990) 6241–6245.
- [39] A.M. Elseman, M.M. Rashad, A.M. Hassan, A.C.S. Sustain, *Chem. Eng.* 4 (2016) 4875–4886.
- [40] M.M. Rashad, A.M. Elseman, A.M. Hassan, *Opt.-Int. J. Light Electron. Opt.* 127 (2016) 9775–9787.
- [41] A. Elseman, A. Shalan, M. Rashad, A. Hassan, *Mater. Sci. Semicond. Process.* 66 (2017) 176–185.
- [42] Z. Zhang, X. Yue, D. Wei, M. Li, P. Fu, B. Xie, D. Song, Y. Li, *RSC Adv.* 5 (2015) 104606–104611.
- [43] P. Cui, P. Fu, D. Wei, M. Li, D. Song, X. Yue, Y. Li, Z. Zhang, Y. Li, J.M. Mbengue, *RSC Adv.* 5 (2015) 75622–75629.



Sajid Sajid received his bachelor's degree in Physics & Mathematics and Master's degree in Physics from Government Post Graduate College Charsadda and Kohat University of Science and Technology KPK, Pakistan, respectively. Recently, he is a Ph.D. scholar at State Key Laboratory of Alternate Electrical Power System with Renewable Energy Sources, School of Renewable Energy, North China Electric Power University, Beijing 102206, China. His current research focuses on understanding mechanisms and fundamental properties of organometal halide perovskite and on developing scalable protocols for high-efficiency perovskite solar cells.



Ahmed Mourtada Elseman is an assistant professor (Post-Doctoral) at Department of Electronic and Magnetic Materials, Central Metallurgical Research & Development Institute (CMRDI), Egypt. He obtained his Ph.D. degree from Chemistry Department, Al-Azhar University, for perovskite solar cells in February 2017. He is a senior researcher at School of Renewable Energy, North China Electric Power University, China. His current research focuses on understanding mechanisms and fundamental properties of organometal halide perovskite and on developing scalable protocols for high-efficiency perovskite solar cells. He is member of Editorial Board at some journal.



Prof. Meicheng Li is the Director of New Energy Materials and PV Technology Center, and the Vice Dean of the School of Renewable Energy, North China Electric Power University. He obtained his Ph.D. at Harbin Institute of Technology in 2001. He worked in University of Cambridge as Research Fellow from 2004 to 2006. He won the Excellent Talents in the New Century by the ministry of education in 2006. His current research topic is the New Energy Materials and Devices, such as solar cells, lithium ion battery. Till now, he contributed more than 200 journal articles. He got almost more than 10 items of awards for the science and technology success. He is an executive fellow of the China Energy Society, fellow of Chinese Society for Optical Engineering.